Aust. J. Math. Anal. Appl.
Vol. **23** (2026), No. 1, Art. 10, 21 pp.
AJMAA

DIRECT SIMULATION VERSUS HOMOGENIZATION FOR OSCILLATORY HYPERBOLIC PROBLEMS: A PRACTICAL ERROR ATLAS VIA FINITE VOLUME METHODS

BIENVENU ONDAMI

Received 11 February, 2026; accepted 4 July, 2026; published 4 August, 2026.

FACULTÉ DES SCIENCES ET TECHNIQUES, UNIVERSITÉ MARIEN NGOUABI, BRAZZAVILLE, RÉPUBLIQUE DU CONGO.
bienvenu.ondami@umng.cg

ABSTRACT. We present a comprehensive numerical study of direct simulation for second order hyperbolic equations with highly oscillatory coefficients. The focus is on regimes where classical homogenization either breaks down or provides unreliable approximations for practical computations. A robust finite volume spatial discretization combined with a fourth order Runge–Kutta time integration method is used to construct a systematic numerical atlas over a wide range of scale separation parameters.

The study compares the behavior of direct numerical simulation and homogenized models in regimes where the microscopic scale is well separated from the macroscopic one, in intermediate regimes where this separation deteriorates, and in situations where fine scale features remain physically relevant. Particular attention is paid to the occurrence of numerical locking in finite volume schemes when critical relations between mesh size and microscopic scale are met.

The results provide practical guidelines for mesh design, identification of reliable parameter ranges for homogenized models, and detection of numerical artefacts. The work highlights the complementarity, rather than the competition, between asymptotic homogenization and direct numerical simulation for multiscale modeling of hyperbolic problems.

Key words and phrases: Hyperbolic equations; Finite volume method; Homogenization; Numerical locking; Multiscale modeling; Runge–Kutta.

2010 *Mathematics Subject Classification.* 35L05, 65M08, 35B27, 65M20, 65L06, 35L15.

ISSN (electronic): 1449-5910

1. INTRODUCTION

Numerical modeling of wave propagation and transport phenomena in heterogeneous media often leads to hyperbolic PDEs with oscillatory coefficients. Classical homogenization provides powerful asymptotic descriptions when the oscillation scale ε is vanishingly small, but real-world applications frequently violate this assumption. In many scenarios, ε is only moderately small, non-periodic, or the solution's fine structure is physically relevant. In such cases, direct numerical simulation (DNS) using sufficient mesh refinement is indispensable.

It is crucial for practitioners to understand not only the respective strengths of homogenization and DNS, but also the transition between their domains of validity. Although FV and FE schemes are well-studied, systematic quantitative analyses of their performance across the full spectrum of ε, including regions of numerical locking and breakdown of scale separation, are rare. This work aims to fill this gap by:

- Providing a detailed numerical atlas that identifies parameter regimes where homogenization fails and DNS remains accurate.
- Demonstrating with transparent error analysis when and why the FV-RK scheme outperforms asymptotic models in capturing multiscale features.
- Delivering practical recommendations to circumvent numerical artifacts, particularly mesh-induced locking.

2. MODEL PROBLEM

In this study, we consider the following model problem:

$$\begin{cases} \Phi^\varepsilon \partial_{tt} u^\varepsilon - \nabla \cdot (K^\varepsilon \nabla u^\varepsilon) = s(x,t) & \text{in } \Omega \times (0,T] \\ u^\varepsilon = 0 & \text{on } \Gamma \times (0,T] \\ u^\varepsilon(x,0) = f(x), \quad \partial_t u^\varepsilon(x,0) = g(x) & \text{in } \Omega \end{cases} \tag{2.1}$$

where Ω, a bounded polygonal convex domain in R^n, with a smooth boundary Γ, $T > 0$ is the final time, Φ^ε represents the porosity of the medium, K^ε is the absolute permeability tensor and u^ε denotes the solute concentration. We will make the following assumptions:

$$\begin{cases} K^\varepsilon(x) := K\left(\frac{x}{\varepsilon}\right),\ K \text{ is a second order and symetric} \\ \text{matrix with } K_{ij} \in L^\infty(Y)\ \ 1 \le i,j \le 2, \\ \forall \xi \in R^n\ \alpha \mid \xi \mid^2 \le < K(x)\xi, \xi > \le\ \beta \mid \xi \mid^2 \ \text{ a.e.} x \in \Omega, \\ 0 < \alpha \le \beta < +\infty, \\ \Phi^\varepsilon(x) := \Phi\left(\frac{x}{\varepsilon}\right),\ \Phi \text{ is a bounded positive, Y-periodic} \\ \text{function with} \\ 0 < \Phi^- \le \Phi(y) \le \Phi^+ < +\infty, \text{and } s \in L^2(\Omega) \times (0,T) \\ f, g \in L^2(\Omega), \end{cases} \tag{2.2}$$

where $< ., . >$ denotes the standard inner product on R^n $(1 \le n \le 2)$, $Y =]0,1[$.

2.1. Justification of assumptions.

The uniform ellipticity condition $(\alpha|\xi|^2 \le \langle K\xi, \xi\rangle \le \beta|\xi|^2)$ guarantees well-posedness of the problem, while the periodicity of K and Φ is essential for homogenization theory. The bounds on Φ ensure non-degenerate porosity, and the L^2-regularity of source/initial data is minimal for energy estimates. These conditions collectively enable both the existence of a unique solution [17, Thm. 2.1] and the derivation of effective homogenized equations.

The existence and uniqueness of u^ε in 2.1 follow directly from assumptions 2.2, as established in classical theory [3, 17]. Using homogenization tools [3, 12, 16, 17], the original problem can be replaced by an effective homogenized problem:

$$\begin{cases} \Phi^* \dfrac{\partial^2 u}{\partial^2 t} - \operatorname{div}\left(K^*(x)\nabla u\right) = s(x,t) \text{ in } \Omega \times (0,T) \\ u = 0 \text{ on } \Gamma \times (0,T) \\ u(x,0) = f(x) \text{ in } \Omega \\ \dfrac{\partial u}{\partial t}(x,0) = g(x) \text{ in } \Omega. \end{cases} \tag{2.3}$$

where $\Phi^* = \int_Y \Phi(y)dy$ and K^* is computed via cell problems [17].

3. APPROXIMATION OF 1D PROBLEM

Throughout this part we assume that the domain Ω is the interval $(0,1)$.

3.1. **Finite Volume (FV) semi-discretization.** By semi-discretization we mean discretization only in space, not in time. We discretize $(0,1)$ into N equal size grid cells of size $h = 1/N$, and define $x_i = h/2 + ih, i = 0, ..., N-1$. So that x_i is the center of the cell $V_i = [x_{i-\frac{1}{2}}, x_{i+\frac{1}{2}}]$, and $h = x_{i+\frac{1}{2}} - x_{i-\frac{1}{2}}$ with $x_{-\frac{1}{2}} = 0, x_{N-\frac{1}{2}} = 1$. Let us denote:

$$u^\varepsilon_{tt} := \frac{\partial^2 u^\varepsilon}{\partial^2 t}, \;\; u^\varepsilon_x := \frac{\partial u^\varepsilon}{\partial x}.$$

One integrates the first equation of problem (2.1) in space over V_i (see, e.g. [15])

$$\int_{x_{i-\frac{1}{2}}}^{x_{i+\frac{1}{2}}} \Phi^\varepsilon u^\varepsilon_{tt}(x,t)dx = \int_{x_{i-\frac{1}{2}}}^{x_{i+\frac{1}{2}}} \left(K^\varepsilon(x)u^\varepsilon_x\right)_x dx + \int_{x_{i-\frac{1}{2}}}^{x_{i+\frac{1}{2}}} s(x,t)dx \tag{3.1}$$

$$\int_{x_{i-\frac{1}{2}}}^{x_{i+\frac{1}{2}}} \left(K^\varepsilon(x)u^\varepsilon_x\right)_x dx = K^\varepsilon(x_{i+\frac{1}{2}})u^\varepsilon_x(x_{i+\frac{1}{2}},t) - K^\varepsilon(x_{i-\frac{1}{2}})u^\varepsilon_x(x_{i-\frac{1}{2}},t) \tag{3.2}$$

$$K^\varepsilon(x_{i+\frac{1}{2}})u^\varepsilon_x(x_{i+\frac{1}{2}},t) \approx K^\varepsilon_{i+\frac{1}{2}}\left[\frac{u^\varepsilon_{i+1}(t) - u^\varepsilon_i(t)}{h}\right] \tag{3.3}$$

$$K^\varepsilon(x_{i-\frac{1}{2}})u^\varepsilon_x(x_{i+\frac{1}{2}},t) \approx K^\varepsilon_{i-\frac{1}{2}}\left[\frac{u^\varepsilon_i(t) - u^\varepsilon_{i-1}(t)}{h}\right] \tag{3.4}$$

Using (3.4),(3.3) and (3.2), (3.1) becomes :

$$\int_{x_{i-\frac{1}{2}}}^{x_{i+\frac{1}{2}}} \Phi^\varepsilon u^\varepsilon_{tt}(x,t)dx \approx \frac{1}{h}\left[K^\varepsilon_{i+\frac{1}{2}}\left(u^\varepsilon_{i+1}(t) - u^\varepsilon_i(t)\right) - K^\varepsilon_{i-\frac{1}{2}}\left(u^\varepsilon_i(t) - u^\varepsilon_{i-1}(t)\right)\right] + \int_{x_{i-\frac{1}{2}}}^{x_{i+\frac{1}{2}}} s(x,t)dx, \tag{3.5}$$

which can also be written as:

$$\frac{d^2 u^\varepsilon_i(t)}{d^2 t} \approx \frac{1}{h^2 \Phi^\varepsilon_i}\left[K^\varepsilon_{i+\frac{1}{2}}u^\varepsilon_{i+1}(t) - \left(K^\varepsilon_{i+\frac{1}{2}} + K^\varepsilon_{i-\frac{1}{2}}\right)u^\varepsilon_i(t) + K^\varepsilon_{i-\frac{1}{2}}u^\varepsilon_{i-1}(t)\right] + \frac{s_i(t)}{\Phi^\varepsilon_i} \tag{3.6}$$

where

$$s_i(t) = \frac{1}{h}\int_{x_{i-\frac{1}{2}}}^{x_{i+\frac{1}{2}}} s(x,t)dx, \quad \Phi^\varepsilon_i u^\varepsilon_i(t) := \frac{1}{h}\int_{x_{i-\frac{1}{2}}}^{x_{i+\frac{1}{2}}} \Phi^\varepsilon u^\varepsilon(x,t)dx$$

To complete the scheme (3.6), we need update formula also for the boundary points $i = 0$ and $i = N-1$ by introduce the ghost cells V_{-1} and V_N wich located just outside the domain. Since

the center of cellsV_0 and V_{N-1} are not on the boundary, we take the average of two cells to approximate the value in between:

$$u^{\varepsilon}_{-1}(t) = -u^{\varepsilon}_0(t); \;\; u^{\varepsilon}_N(t) = -u^{\varepsilon}_{N-1}(t). \tag{3.7}$$

For $i = 0$, (3.6) becomes by using (3.7):

$$\frac{d^2u^{\varepsilon}_0(t)}{d^2t} \approx \frac{1}{h^2\Phi^{\varepsilon}_0}\left[-\left(K^{\varepsilon}_{\frac{1}{2}} + 2K^{\varepsilon}_{-\frac{1}{2}}\right)u^{\varepsilon}_0(t) + K^{\varepsilon}_{\frac{1}{2}}u^{\varepsilon}_1(t)\right] + \frac{s_0(t)}{\Phi^{\varepsilon}_0} \tag{3.8}$$

For $i = N-1$, (3.6) becomes by using (3.7):

$$\frac{d^2u^{\varepsilon}_{N-1}(t)}{d^2t} \approx \frac{1}{h^2\Phi^{\varepsilon}_{N-1}}\left[K^{\varepsilon}_{N-\frac{3}{2}}u^{\varepsilon}_{N-2}(t) - \left(2K^{\varepsilon}_{N-\frac{1}{2}} + K^{\varepsilon}_{N-\frac{3}{2}}\right)u^{\varepsilon}_{N-1}(t)\right] + \frac{s_{N-1}(t)}{\Phi^{\varepsilon}_{N-1}} \tag{3.9}$$

From (3.6),(3.8) and (3.9) using (3.7), one gets for $1 \leq i \leq N-1$, the folowing ODE:

$$\begin{cases} u^{\varepsilon h}_{tt}(x_i,t) = K^{\varepsilon h}u^{\varepsilon h}(x_i,t) + s^{\varepsilon h}(x_i,t), \\ u^{\varepsilon h}(0,t) = u^{\varepsilon h}(1,t) = 0, \\ u^{\varepsilon h}(x_i,0) = F, \\ u^{\varepsilon h}_t(x_i,0) = G. \end{cases} \tag{3.10}$$

3.2. **Runge-Kutta discretization .** We recast the second-order system (3.10) as a first-order problem to facilitate time integration via a fourth-order Runge-Kutta scheme, leveraging its stability for stiff ODEs [24].

$$\begin{cases} v^{\varepsilon h}(x_i,t) = u^{\varepsilon h}_t(x_i,t), \\ v^{\varepsilon h}_t(x_i,t) = K^{\varepsilon h}u^{\varepsilon h}(x_i,t) + s^{\varepsilon h}(x_i,t), \\ u^{\varepsilon h}(0,t) = u^{\varepsilon h}(1,t) = 0, \\ u^{\varepsilon h}(x_i,0) = F, \\ v^{\varepsilon h}(x_i,0) = G. \end{cases} \tag{3.11}$$

Let be $\Delta t = \frac{T}{M}$ $(M > 0)$, the time step and $t_n = n\Delta t$. We denote $u^{\varepsilon n}$ as the fourth-order Runge-Kutta approximation of $u^{\varepsilon h}(x_i,t_n)$ and $v^{\varepsilon n}(x_i,t_n)$ as the approximation of $v^{\varepsilon h}(x_i,t)$.

3.3. **Numerical simulations .** In this section, we present numerical results obtained using the adaptive Runge–Kutta scheme implemented in Scilab. These simulations compare the exact solution with the numerical approximations obtained by solving both the original problem, Problem (2.1), and its homogenized counterpart, Problem (2.3), using the MOL–FV–RK method described previously. In the figures presented below, *EXACT* refers to the analytical solution (u^{ε}), *DNS* denotes the direct numerical solution of the original problem ($u^{\varepsilon h}$), and *HOMOG* designates the solution of the homogenized problem (u).

It is standard in the numerical homogenization literature to allow the source term or the initial condition to depend on ε for the construction of explicit analytical benchmarks (see, e.g., [26] and [27]). Therefore, the simulations were performed using the function g in Problem (2.1) dependent on ε.

$$K^{\varepsilon}(x) = \frac{1}{a + b\sin\left(\dfrac{2\pi x}{\varepsilon}\right)}, \;\; \Phi^{\varepsilon}(x) = 2.1 + 0.5\left[\sin\left(\frac{2\pi x}{\varepsilon}\right) + \cos\left(\frac{2\pi x}{\varepsilon}\right)\right], \tag{3.12}$$

$$0 < b < a, \;\; \Phi^* = 2.1, \;\; K^* = \frac{1}{a}, \;\; s(x,t) = t, \;\; f(x) = 0.$$

The exact solution $u_\varepsilon(x)$ of the elliptic problem

$$-\nabla \cdot (K^\varepsilon \nabla u_\varepsilon) = 1 \tag{3.13}$$

is given by [22]:

$$u_\varepsilon(x) = -\frac{ax^2}{2} + \left[aC_1^\varepsilon + \frac{b\varepsilon}{2\pi}\cos\left(2\pi\frac{x}{\varepsilon}\right)\right]x - \frac{b\varepsilon}{2\pi}\left[C_1^\varepsilon \cos\left(2\pi\frac{x}{\varepsilon}\right) + \frac{\varepsilon}{2\pi}\sin\left(2\pi\frac{x}{\varepsilon}\right)\right] + C_2^\varepsilon$$

where the constants C_1^ε and C_2^ε are determined by:

$$C_1^\varepsilon = \frac{\frac{a}{2} - \frac{b\varepsilon}{2\pi}\left[\cos\left(\frac{2\pi}{\varepsilon}\right) - \frac{\varepsilon}{2\pi}\sin\left(\frac{2\pi}{\varepsilon}\right)\right]}{a + \frac{b\varepsilon}{2\pi}\left[1 - \cos\left(\frac{2\pi}{\varepsilon}\right)\right]}$$

$$C_2^\varepsilon = \frac{b\varepsilon}{2\pi}C_1^\varepsilon.$$

$$\frac{\partial u^\varepsilon}{\partial t}(x,0) = g_\varepsilon = u_\varepsilon(x).$$

Therefore, The exact solution of the hyperbolic problem (2.1) is constructed as:

$$u^\varepsilon(x,t) = t \cdot u_\varepsilon(x).$$

All numerical tests were performed with the parameters $a = 1$ and $b = 0.5$.

For the homogenized Problem (2.3), the initial condition on the first time derivative g is given by

$$g(x) = u^*(x) = \frac{1}{2}x(1-x), \text{where } u^* \text{ is the homogenized solution of Problem (3.13).}$$

3.3.1. *First test series: pre-homogenization regime ($h < \varepsilon$)* . In this first test series, we investigate the pre-homogenization regime corresponding to $h < \varepsilon$, where the computational grid is fine enough to resolve the oscillatory pattern of the coefficient $K^\varepsilon(x)$. This configuration allows us to assess the accuracy of the direct numerical simulation (DNS) and to quantify the discrepancy between the exact and homogenized solutions when microscale effects are explicitly captured. The following tables and figures summarize the evolution of the L^∞ and L^2 errors with respect to h.

Table 3.1: Comparison between u^ε vs $u^{\varepsilon h}$, $\varepsilon = 1.71 \times 10^{-1}$, $\Delta t = 0.1$, $T = 1$

h	$1/32$	$1/128$	$1/512$	$1/1024$	$1/2048$	$1/4096$	$1/8192$
$\|u^\varepsilon - u^{\varepsilon h}\|_\infty$	9.05e-04	6.04e-05	3.79e-06	9.51e-07	2.38e-07	5.95e-08	1.50e-08
$\|u^\varepsilon - u^{\varepsilon h}\|_{L^2}$	3.97e-04	2.44e-05	1.52e-06	3.81e-07	9.52e-08	2.38e-08	5.95e-09

Table 3.2: Comparison between u^ε vs u^h, $\varepsilon = 1.71 \times 10^{-1}$, $\Delta t = 0.1$, $T = 1$

h	$1/32$	$1/128$	$1/512$	$1/1024$	$1/2048$	$1/4096$	$1/8192$
$\|u^\varepsilon - u^h\|_\infty$	1.10e-02	1.12e-02	1.12e-02	1.12e-02	1.12e-02	1.12e-02	1.12e-02
$\|u^\varepsilon - u^h\|_{L^2}$	4.42e-03	4.44e-03	4.44e-03	4.44e-03	4.44e-03	4.44e-03	4.44e-03

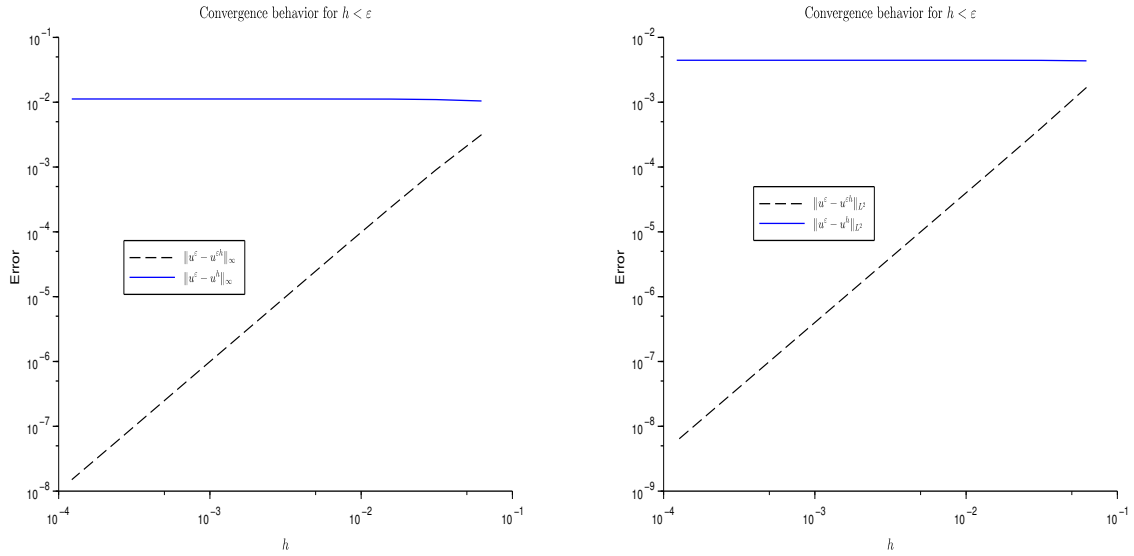

Figure 1: Error curves for the case $h < \varepsilon$. Left: L^∞-norm errors between the exact solution u^ε, the direct numerical solution $u^{\varepsilon h}$ (DNS), and the homogenized solution u (HOMOG). Right: corresponding L^2-norm errors for the same comparisons. The plots illustrate the convergence of the MOL–FV–RK scheme and the accuracy limits of the homogenized model in the pre-homogenization regime.

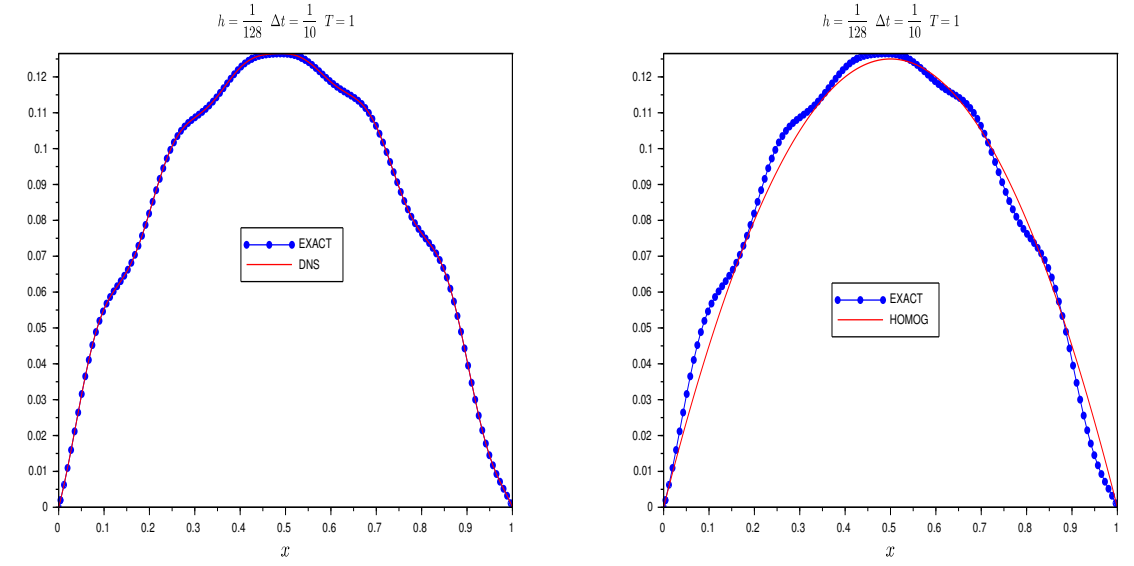

Figure 2: Comparison of spatial profiles between the numerical and homogenized solutions for the case $h < \varepsilon$. Left: comparison between the exact solution u^ε and the direct numerical solution $u^{\varepsilon h}$ (DNS). Right: comparison between the exact solution u^ε and the homogenized solution u. For this pre-homogenization regime, the DNS captures the oscillatory pattern of the exact solution, while the homogenized model smooths out these fine-scale variations.

3.3.2. *Second test series: post-homogenization regime ($h > \varepsilon$).* The second test series focuses on the post-homogenization regime, where $h > \varepsilon$. In this case, the mesh size exceeds the characteristic oscillation scale, and the fine variations of $K^\varepsilon(x)$ are no longer resolved at the discrete level. This regime is used to verify that the homogenized model provides an accurate

macroscopic approximation and that the DNS solution converges toward the same effective behavior. The subsequent tables and plots present the corresponding L^∞ and L^2 error trends as functions of h.

Although the DNS error is not strictly monotone with respect to h it remains small and exhibits an overall decreasing trend toward the homogenized limit. This non-monotonic behavior can be attributed to residual numerical resonance effects when the discretization size h becomes commensurable with the microscopic scale ε.

Table 3.3: Comparison between u^ε vs $u^{\varepsilon h}$, $\varepsilon = 1.71 \times 10^{-4}$, $\Delta t = 0.1$, $T = 1$

h	$1/32$	$1/128$	$1/256$	$1/512$	$1/1024$	$1/2048$	$1/4096$
$\|u^\varepsilon - u^{\varepsilon h}\|_\infty$	7.42e-03	1.77e-03	1.86e-03	3.06e-04	2.55e-04	4.56e-03	3.83e-05
$\|u^\varepsilon - u^{\varepsilon h}\|_{L^2}$	3.35e-03	6.31e-04	7.25e-04	1.12e-04	9.15e-05	1.01e-04	1.56e-05

Table 3.4: Comparison between u^ε vs u^h, $\varepsilon = 1.71 \times 10^{-4}$, $\Delta t = 0.1$, $T = 1$

h	$1/32$	$1/128$	$1/256$	$1/512$	$1/1024$	$1/2048$	$1/4096$
$\|u^\varepsilon - u^h\|_\infty$	1.32e-04	1.97e-05	1.50e-05	1.31e-05	1.30e-05	1.33e-05	1.32e-05
$\|u^\varepsilon - u^h\|_{L^2}$	8.62e-05	7.06e-06	4.91e-06	4.74e-06	4.74e-06	4.75e-06	4.74e-06

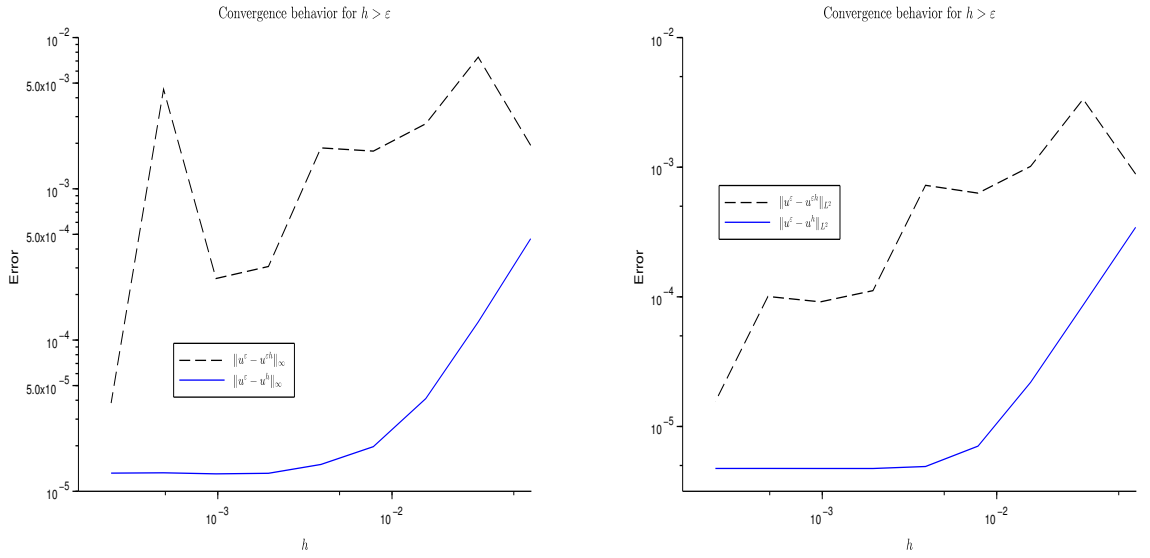

Figure 3: Error curves for the case $h > \varepsilon$. Left: L^∞-norm errors between the exact solution u^ε, the direct numerical solution $u^{\varepsilon h}$ (DNS), and the homogenized solution u (Homog). Right: corresponding L^2-norm errors for the same comparisons. Although local oscillations appear in the DNS error the overall trend confirms convergence of both the DNS and the homogenized solutions toward the same asymptotic limit in this post-homogenization regime.

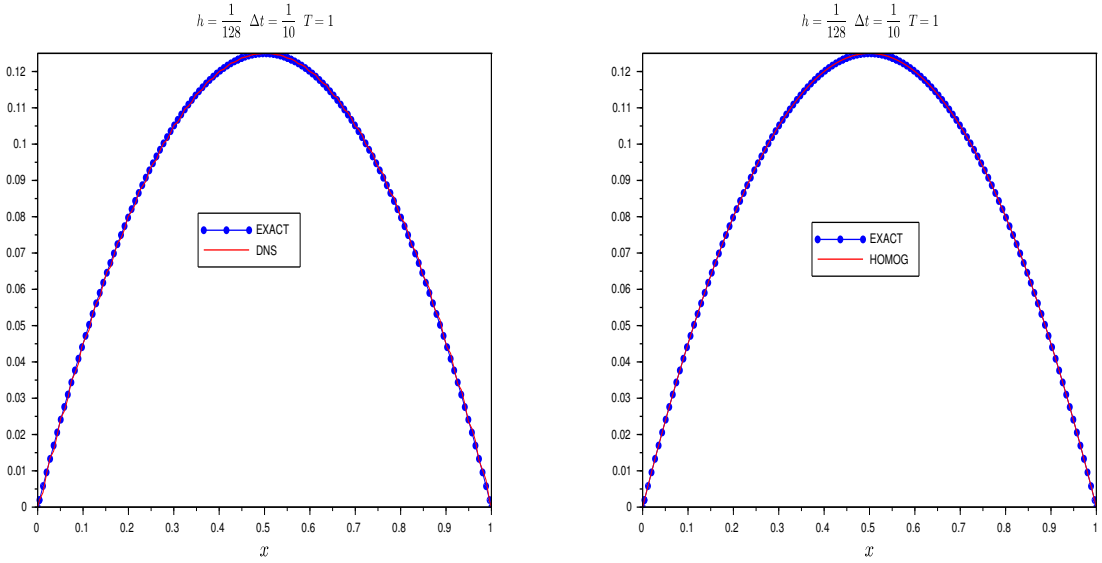

Figure 4: Comparison of spatial profiles between the direct numerical solution ($u^{\varepsilon h}$, DNS) and the homogenized solution (u, Homog) at final time $T = 1$ for the case $h > \varepsilon$. The left plot shows the comparison between the exact solution u^{ε} and the DNS solution, while the right plot compares u^{ε} with the homogenized model u. Both DNS and homogenized solutions provide an excellent approximation of the exact solution, confirming the accuracy of the numerical approach and the validity of the homogenized model in the post-homogenization regime.

3.3.3. *Numerical Locking Phenomenon.* A third test series is devoted to the investigation of a *numerical locking effect* that may occur when the mesh size h and the microscale parameter ε are commensurable, that is, when their ratio satisfies $h/\varepsilon = n$ with n an integer. In such cases, the periodic structure of the coefficients K^{ε} and Φ^{ε} is sampled at precisely the same relative positions in each cell, which can lead to pathological numerical behavior.

Specifically, when $h/\varepsilon = n$, the discrete numerical operator in the direct simulation (DNS) effectively replaces the oscillatory coefficients $K^{\varepsilon}(x)$ and $\Phi^{\varepsilon}(x)$ by constants obtained by freezing their values at $x/\varepsilon = n$. If this particular value does not correspond to the correct macroscopic average, the resulting numerical solution may become completely unrelated to both the exact microscopic solution and the homogenized one. This phenomenon may thus be seen as a form of *numerical resonance* or *locking* induced by the artificial periodic synchronization between grid points and the microstructure. This observation can be rigorously stated in the following proposition, which formalizes the effect of the commensurability condition $h/\varepsilon = n$ on the discrete problem.

Proposition 3.1 (Numerical Locking by Commensurability)**.** *Let the oscillatory coefficients be $K^{\varepsilon}(x) = K(x/\varepsilon)$ and $\Phi^{\varepsilon}(x) = \Phi(x/\varepsilon)$ with K and Φ being Y-periodic. If the mesh satisfies $h/\varepsilon = n \in \mathbb{N}$, the numerical scheme samples K and Φ at identical phase positions in every cell, so that the discrete problem is equivalent to one with constant coefficients*

$$\tilde{K} = K(n), \qquad \tilde{\Phi} = \Phi(n).$$

Unless $(\tilde{K}, \tilde{\Phi}) = (K_*, \Phi_*)$, the resulting discrete (DNS) solution differs completely from both the exact oscillatory and the homogenized solution. Conversely, if the coefficients satisfy $K(n) = K_*$ and $\Phi(n) = \Phi_*$, then the DNS solution coincides with the homogenized and the exact solutions.

Remark 3.1. The proof of this proposition follows directly from the periodic sampling mechanism of the coefficients. When $h/\varepsilon = n$, each grid point coincides with an identical phase of the periodic functions, so that the discrete operator acts effectively with constant coefficients. As the argument is straightforward, it is omitted here. However, the numerical experiments presented below clearly confirm the two contrasting cases highlighted in the proposition.

Two representative numerical examples are given to illustrate these effects:

- **Example 1:** The coefficients defined by (3.12) yield the situation where the commensurability condition $h/\varepsilon = n$ does not disturb the numerical behavior. In this configuration, the discrete sampling of $K^\varepsilon(x)$ and $\Phi^\varepsilon(x)$ exactly matches the homogenized coefficients (K_*, Φ_*). Consequently, the direct numerical solution (DNS) coincides perfectly with both the exact oscillatory and homogenized solutions. This behavior is clearly visible in Figure 5, where both plots show an overlap of the three curves.

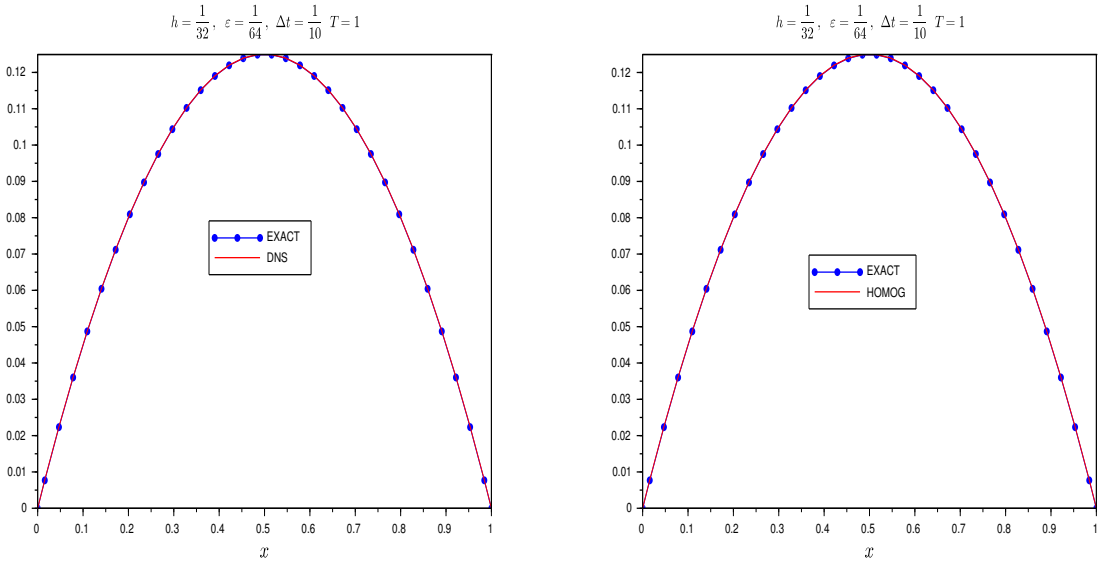

Figure 5: Illustration of the non-locking case under the commensurability condition $h/\varepsilon = n$. Left: comparison between the exact solution u^ε, the direct numerical solution ($u^{\varepsilon h}$, DNS), and the homogenized solution u — all three curves coincide. Right: zoomed-in view confirming the perfect overlap, showing that the discrete sampling effectively reproduces the homogenized coefficients (K_*, Φ_*).

- **Example 2:** When the coefficients are given by

$$K^\varepsilon(x) = \frac{1}{1 + 0.5\big[\sin(2\pi x/\varepsilon) + \cos(2\pi x/\varepsilon)\big]}, \qquad \Phi^\varepsilon(x) \text{ as in (3.12)},$$

the mesh–microstructure synchronization $h/\varepsilon = n$ leads to a complete *numerical locking*. In this case, the coefficients sampled by the discrete operator do not correspond to the homogenized pair (K_*, Φ_*), which causes the DNS solution to deviate strongly from both the exact and homogenized profiles. Figure 6 highlights this inconsistency through visibly distinct curves.

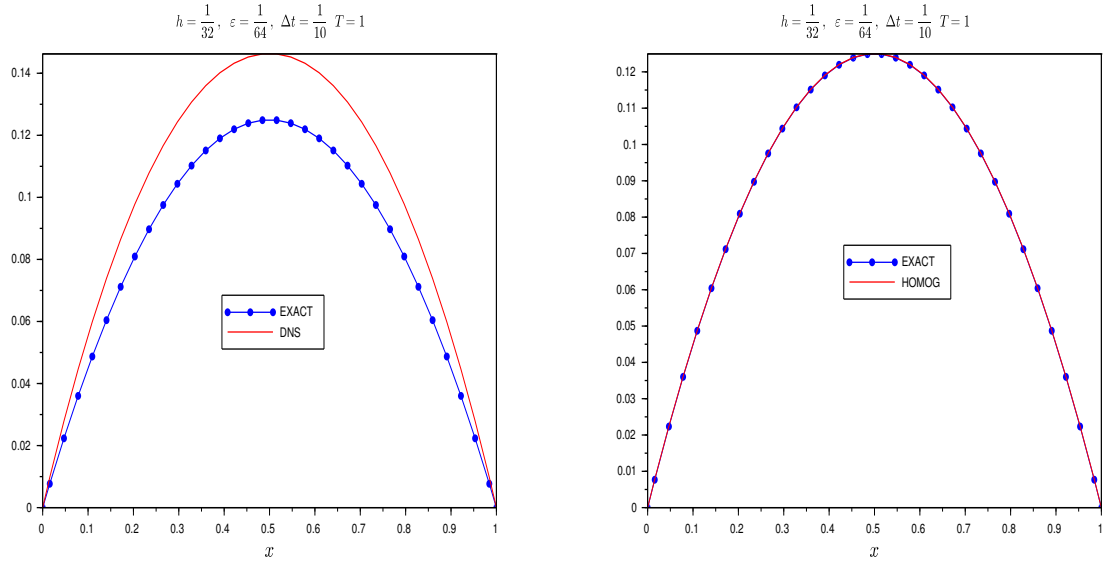

Figure 6: Illustration of the locking case under the commensurability condition $h/\varepsilon = n$. Left: comparison of the exact solution u^ε and the direct numerical solution $u^{\varepsilon h}$ (DNS) showing clear divergence due to sampling at non-representative coefficient values. Right: comparison of u^ε with the homogenized solution u, revealing that the two reference solutions remain consistent while the DNS solution exhibits an erroneous numerical resonance pattern.

4. APPROXIMATION OF 2D PROBLEM

Because simplification reasons we limit the study to the case of a diagonal K matrix, and $\Omega = (0,1) \times (0,1)$.

4.1. **FV semi-discrezation .** We introduce the grid for the cell-centered finite volume scheme for which we partition Ω in the x and y directions as:
$0 = x_{\frac{1}{2}} < x_1 < x_{\frac{3}{2}} < x_2 < ... < x_{i-\frac{1}{2}} < x_i < x_{N+\frac{1}{2}} = 1,$
$0 = y_{\frac{1}{2}} < y_1 < y_{\frac{3}{2}} < y_2 < ... < y_{j-\frac{1}{2}} < y_i < y_{N+\frac{1}{2}} = 1.$
We then define the cells (finite volumes) to be the square:
$V_{i,j} = \left(x_{i-\frac{1}{2}}, x_{i+\frac{1}{2}}\right) \times \left(y_{j-\frac{1}{2}}, y_{j+\frac{1}{2}}\right), 1 \le i,j \le N-1$, with the center (x_i, y_j) and nodes of half indices. Let

$$\begin{cases} h = x_{i+1} - x_i = y_{j+1} - y_j,\ 1 \le i,j \le N-1, \\ h = x_{i+\frac{1}{2}} - x_{i-\frac{1}{2}} = y_{i+\frac{1}{2}} - y_{i-\frac{1}{2}},\ 1 \le i,j \le N. \end{cases} \tag{4.1}$$

The grid steps in the x and y directions are given by (4.1).

We next discretize the problem (2.1) by the cell-centered finite volumes scheme, only in space, not in time. The unknowns approximate the average of the solution over a grid cell. More precisely, we let be $u^\varepsilon_{ij}(t)$ the approximation given by

$$u^\varepsilon_{ij}(t) := \frac{1}{h^2} \int_{V_{i,j}} u^\varepsilon(x,y,t)dxdy. \tag{4.2}$$

To enforce the boundary conditions across the outher boundaries, we define the fictitious bounday cells where the ghost values (see, e.g. [14]):

$\left\{u^\varepsilon_{0,j}(t),\ u^\varepsilon_{N+1,j}(t),\ j = 1, ..., N\right\}$, and $\left\{u^\varepsilon_{i,0}(t),\ u^\varepsilon_{i,N+1}(t),\ i = 1, ..., N\right\}$ are defined.

We set:

$$V_{0,j}=\left(x_{-\frac{1}{2}},x_{\frac{1}{2}}\right)\times\left(y_{j-\frac{1}{2}},y_{j+\frac{1}{2}}\right),\ V_{N+1,j}=\left(x_{N+\frac{1}{2}},x_{N+\frac{3}{2}}\right)\times\left(y_{j-\frac{1}{2}},y_{j+\frac{1}{2}}\right),$$

$$V_{i,0}=\left(x_{i-\frac{1}{2}},x_{i+\frac{1}{2}}\right)\times\left(y_{-\frac{1}{2}},y_{\frac{1}{2}}\right),\ V_{i,N+1}=\left(x_{i-\frac{1}{2}},x_{i+\frac{1}{2}}\right)\times\left(y_{N+\frac{1}{2}},y_{N+\frac{3}{2}}\right),$$

where $1\leq i,j\leq N$ and

$$x_{-\frac{1}{2}}=-x_{\frac{3}{2}},\ x_{N+\frac{3}{2}}=2-x_{N-\frac{1}{2}},\ y_{-\frac{1}{2}}=-y_{\frac{3}{2}},\ y_{N+\frac{3}{2}}=2-y_{N-\frac{1}{2}}.$$

Let

$$\Phi_{ij}^{\varepsilon}u_{ij}^{\varepsilon}(t):=\frac{1}{h^2}\int_{V_{i,j}}\Phi^{\varepsilon}u^{\varepsilon}(x,y,t)dxdy, \tag{4.3}$$

where

$$\Phi_{ij}^{\varepsilon}:=\Phi^{\varepsilon}\left(x_i,y_j\right),\ \text{and}\ u_{ij}^{\varepsilon}\ \text{is given by}\ (4.2). \tag{4.4}$$

Equations (4.3) and (4.4) define the discrete coefficients and unknowns.

Using the divergence theorem to integrate the first equation of (2.1) over V_{ij}, divising by h^2 and using (4.3) we get:

$$\begin{aligned}\Phi_{ij}^{\varepsilon}\frac{\partial^2u_{ij}^{\varepsilon}(t)}{\partial^2t}&=\frac{1}{h^2}\int_{y_{j-\frac{1}{2}}}^{y_{j+\frac{1}{2}}}K_{11}^{\varepsilon}(x_{i+\frac{1}{2}},y)u_x^{\varepsilon}(x_{i+\frac{1}{2}},y,t)dy-\frac{1}{h^2}\int_{y_{j-\frac{1}{2}}}^{y_{j+\frac{1}{2}}}K_{11}^{\varepsilon}(x_{i-\frac{1}{2}},y)u_x^{\varepsilon}(x_{i-\frac{1}{2}},y,t)dy\\&+\frac{1}{h^2}\int_{x_{i-\frac{1}{2}}}^{x_{i+\frac{1}{2}}}K_{22}^{\varepsilon}(x,y_{j+\frac{1}{2}})u_y^{\varepsilon}(x,y_{j+\frac{1}{2}},t)dx-\frac{1}{h^2}\int_{x_{i-\frac{1}{2}}}^{x_{i+\frac{1}{2}}}K_{22}^{\varepsilon}(x,y_{j-\frac{1}{2}})u_y^{\varepsilon}(x,y_{j-\frac{1}{2}},t)dx\\&+\frac{1}{h^2}\int_{x_{i-\frac{1}{2}}}^{x_{i+\frac{1}{2}}}\int_{y_{j-\frac{1}{2}}}^{y_{j+\frac{1}{2}}}s(x,y,t)dxdy\end{aligned} \tag{4.5}$$

Equation (4.5) is the starting point for the finite volume discretization. The last term of the right hand side can be approximated by $s_{i,j}(t)=s\left(x_i,y_j,t\right)$.
We're only going to approximate the first integral on the right hand side in (4.5) , the others terms can be treated in the same way.

$$\begin{aligned}\int_{y_{j-\frac{1}{2}}}^{y_{j+\frac{1}{2}}}K_{11}^{\varepsilon}(x_{i+\frac{1}{2}},y)u_x^{\varepsilon}(x_{i+\frac{1}{2}},y,t)dy&\approx\int_{y_{j-\frac{1}{2}}}^{y_{j+\frac{1}{2}}}K_{11}^{\varepsilon}(x_{i+\frac{1}{2}},y)\left(\frac{u^{\varepsilon}\left(x_{i+1},y,t\right)-u^{\varepsilon}\left(x_i,y,t\right)}{h}\right)dy\\&\approx K_{11}^{\varepsilon}(x_{i+\frac{1}{2}},y_j)\left(u_{i+1,j}^{\varepsilon}-u_{i,j}^{\varepsilon}\right),\ \text{on interior cells}\ \ (2\leq i,j\leq N-1).\end{aligned} \tag{4.6}$$

Note that we have made two approximations at this step. Firstly, a piecewise constant approximation to the $y-$dependence of $K_{11}^{\varepsilon}(x,y)$. Along each volume boundary we have replaced $K_{11}^{\varepsilon}(x_{i+\frac{1}{2}},y)$ by the midpoint (in y) value $K_{11}^{\varepsilon}(x_{i+\frac{1}{2}},y_j)$. Secondly, we have made a linear approximation to the $x-$dependence of u^{ε}. By similar reasoning, we get, on interior cells:

$$\int_{y_{j-\frac{1}{2}}}^{y_{j+\frac{1}{2}}}K_{11}^{\varepsilon}(x_{i-\frac{1}{2}},y)u_x^{\varepsilon}(x_{i-\frac{1}{2}},y,t)dy\approx K_{11}^{\varepsilon}(x_{i-\frac{1}{2}},y_j)\left(u_{i,j}^{\varepsilon}-u_{i-1,j}^{\varepsilon}\right), \tag{4.7}$$

$$\int_{x_{i-\frac{1}{2}}}^{x_{i+\frac{1}{2}}}K_{22}^{\varepsilon}(x,y_{j+\frac{1}{2}})u_y^{\varepsilon}(x,y_{j+\frac{1}{2}},t)dx\approx K_{22}^{\varepsilon}(x_i,y_{j+\frac{1}{2}})\left(u_{i,j+1}^{\varepsilon}-u_{i,j}^{\varepsilon}\right) \tag{4.8}$$

$$\int_{x_{i-\frac{1}{2}}}^{x_{i+\frac{1}{2}}} K_{22}^{\varepsilon}(x, y_{j-\frac{1}{2}}) u_x^{\varepsilon}(x_{i-\frac{1}{2}}, y, t) dx \approx K_{22}^{\varepsilon}(x_i, y_{j-\frac{1}{2}}) \left(u_{i,j}^{\varepsilon} - u_{i,j-1}^{\varepsilon}\right). \tag{4.9}$$

The approximations (4.6)–(4.9) are used to discretize the flux integrals.

Using (4.5)–(4.9), we obtain the semi-discrete scheme:

$$\begin{aligned}\frac{d^2 u_{ij}^{\varepsilon}(t)}{dt} &= \frac{K_{11}^{\varepsilon}(x_{i+\frac{1}{2}}, y_j)}{\Phi_{ij}^{\varepsilon} h^2}\left(u_{i+1,j}^{\varepsilon} - u_{i,j}^{\varepsilon}\right) - \frac{K_{11}^{\varepsilon}(x_{i-\frac{1}{2}}, y_j)}{\Phi_{ij}^{\varepsilon} h^2}\left(u_{i,j}^{\varepsilon} - u_{i-1,j}^{\varepsilon}\right) \\ &+ \frac{K_{22}^{\varepsilon}(x_i, y_{j+\frac{1}{2}})}{\Phi_{ij}^{\varepsilon} h^2}\left(u_{i,j+1}^{\varepsilon} - u_{i,j}^{\varepsilon}\right) - \frac{K_{22}^{\varepsilon}(x_i, y_{j-\frac{1}{2}})}{\Phi_{ij}^{\varepsilon} h^2}\left(u_{i,j}^{\varepsilon} - u_{i,j-1}^{\varepsilon}\right) + \frac{s_{ij}(t)}{\Phi_{ij}^{\varepsilon}}\end{aligned} \tag{4.10}$$

After grouping simular terms in (4.10) we get, on interior cells ($2 \leq i, j \leq N-1$) :

$$\begin{aligned}\frac{d^2 u_{i,j}^{\varepsilon}(t)}{d^2 t} &= \frac{K_{11}^{\varepsilon}(x_{i-\frac{1}{2}}, y_j)}{\Phi_{ij}^{\varepsilon} h^2} u_{i-1,j}^{\varepsilon} + \frac{K_{22}^{\varepsilon}(x_i, y_{j-\frac{1}{2}})}{\Phi_{ij}^{\varepsilon} h^2} u_{i,j-1}^{\varepsilon} + \frac{K_{22}^{\varepsilon}(x_i, y_{j+\frac{1}{2}})}{\Phi_{ij}^{\varepsilon} h^2} u_{i,j+1}^{\varepsilon} + \frac{K_{11}^{\varepsilon}(x_{i+\frac{1}{2}}, y_j)}{\Phi_{ij}^{\varepsilon} h^2} u_{i+1,j}^{\varepsilon} \\ &- \frac{K_{11}^{\varepsilon}(x_{i+\frac{1}{2}}, y_j) + K_{11}^{\varepsilon}(x_{i-\frac{1}{2}}, y_j) + K_{22}^{\varepsilon}(x_i, y_{j+\frac{1}{2}}) + K_{22}^{\varepsilon}(x_i, y_{j-\frac{1}{2}})}{\Phi_{ij}^{\varepsilon} h^2} u_{i,j}^{\varepsilon} + \frac{s_{i,j}(t)}{\Phi_{ij}^{\varepsilon}}.\end{aligned} \tag{4.11}$$

Equation (4.11) is the final form of the semi-discrete finite volume scheme.

To enforce the boundary conditions, a standard approach is to make use of ghost cells with ghost values defined by

$$u_{0,j}^{\varepsilon} = -u_{1,j}^{\varepsilon},\ u_{i,0}^{\varepsilon} = -u_{i,1}^{\varepsilon},\ u_{N+1,j}^{\varepsilon} = -u_{N,j}^{\varepsilon},\ u_{i,N+1}^{\varepsilon} = -u_{i,N}^{\varepsilon}\ 1 \leq i, j \leq N. \tag{4.12}$$

After completing the scheme (4.11) by updating formula for the boundary cells by using (4.12) as in [5, 8], one gets an ODE of the form (3.10) which we write as:

$$\begin{cases} u_{tt}^{\varepsilon h}(t) = K^{\varepsilon h} u^{\varepsilon h}(t) + s^{\varepsilon}(t), \\ u^{\varepsilon h} = 0 \ \text{ on } \ \Gamma \cap \Omega_h, \\ u^{\varepsilon h}(0) = F, \\ u_t^{\varepsilon h}(0) = G. \end{cases} \tag{4.13}$$

where $K^{\varepsilon h}$ is a square matrix of order N^2. The resolution of system (4.13) is done by the Runge-Kutta method as for system (3.11).

4.2. **Numerical simulations.** The simulations were carried out with following data:

$$K_{11}^{\varepsilon}(x, y) = \frac{1}{a + b\sin\left(2\pi\frac{x}{\varepsilon}\right)},\ \ K_{22}^{\varepsilon}(x, y) = \frac{1}{c + d\sin\left(2\pi\frac{y}{\varepsilon}\right)}$$

$$\Phi\left(x, y\right) = \frac{1}{\left[1 + \frac{1}{2}\sin(2\pi x)\right]\left[1 + \frac{1}{2}\sin(2\pi y)\right]}.$$

We define the exact solution as the sum of 1D solutions:

$$v^{\varepsilon}(x, y) = u_1^{\varepsilon}(x) * u_2^{\varepsilon}(y)$$

where $u_\varepsilon^1(x)$ and $u_\varepsilon^2(y)$ are the 1D solutions of:

$$-\frac{d}{dx}\left(K_{11}^\varepsilon(x)\frac{du_1^\varepsilon}{dx}\right) = 1 \quad \text{in } (0,1)$$
$$-\frac{d}{dy}\left(K_{22}^\varepsilon(y)\frac{du_2^\varepsilon}{dy}\right) = 1 \quad \text{in } (0,1)$$

with homogeneous Dirichlet boundary conditions. Therefore $v^\varepsilon = 0$ on $\Gamma = \partial\Omega$ where $\Omega = (0,1)\times(0,1)$.
We define $u^\varepsilon(x,y,t) = tv^\varepsilon(x,y)$, the exact solution of Problem (2.1). Therefore

$$s(x,y,t) = s^\varepsilon(x,y,t)t\left[u_1^\varepsilon(x) + u_2^\varepsilon(y)\right], \;\; u^\varepsilon(x,y,0) = 0, \;\; \frac{\partial u^\varepsilon}{\partial t}(x,y,0) = v^\varepsilon(x,y).$$

4.3. **Two–dimensional numerical simulations.** In this section, we investigate the performance of the MOL–FV–RK scheme for the two–dimensional version of Problem 2.1, using the manufactured solution and data defined above. The oscillatory reference solution u^ε is available in closed form, while the homogenized problem is solved numerically, so that all comparisons involving the homogenized model are carried out between the analytical oscillatory solution and the numerical approximation u^h of the homogenized Problem 2.3.

The spatial discretization is performed on a uniform Cartesian grid of the unit square $\Omega = (0,1)\times(0,1)$ with $N\times N$ control volumes, and time integration uses the same explicit fourth–order Runge–Kutta method as in the one–dimensional tests. For each configuration, the mesh size is $h = 1/N$ and the oscillation parameter ε is kept fixed unless stated otherwise. We denote by u_h^ε the DNS solution of the original oscillatory problem, and u^ε the exact oscillatory solution. The errors are measured in the discrete L^∞– and L^2–norms at the final time $T = 1$.

4.3.1. *Pre–homogenization regime in 2D: $h < \varepsilon$.* We first consider a pre–homogenization configuration where the mesh is fine enough to resolve the microscopic oscillations of the coefficients. In this regime, the DNS solution u_h^ε is expected to approximate accurately the exact oscillatory solution u^ε, whereas the homogenized model, even when solved numerically, cannot reproduce the fine–scale oscillations and should therefore exhibit a larger discrepancy with u^ε.

To illustrate this regime, we fix $\varepsilon = 1.5\times10^{-1}$ and use a family of meshes with $N \in \{16, 32, 64, 128, 192\}$, corresponding to $h \in \{6.25\times10^{-2}, 3.125\times10^{-2}, 1.5625\times10^{-2}, 7.8125\times10^{-3}, 5.2083\times10^{-3}\}$; in all these cases one has $h < \varepsilon$. The resulting errors for the DNS solution of the original problem and for the numerical solution of the homogenized problem are reported in Table 4.1.

Table 4.1: 2D pre–homogenization regime ($\varepsilon = 1.5\times10^{-1}$): errors between the DNS solution $u^{\varepsilon h}$ of the oscillatory problem and the exact oscillatory solution u^ε, and between the DNS solution u^h of the homogenized problem and u^ε, at final time $T = 1$.

N	h	$\|u^{\varepsilon h} - u^\varepsilon\|_{L^\infty}$	$\|u^{\varepsilon h} - u^\varepsilon\|_{L^2}$	$\|u^h - u^\varepsilon\|_{L^\infty}$	$\|u^h - u^\varepsilon\|_{L^2}$
16	6.25×10^{-2}	1.01×10^{-3}	4.21×10^{-4}	8.98×10^{-3}	4.98×10^{-3}
32	3.125×10^{-2}	1.20×10^{-3}	3.44×10^{-4}	9.01×10^{-3}	4.99×10^{-3}
64	1.5625×10^{-2}	1.21×10^{-3}	3.37×10^{-4}	9.02×10^{-3}	4.99×10^{-3}
128	7.8125×10^{-3}	1.23×10^{-3}	3.36×10^{-4}	9.02×10^{-3}	5.00×10^{-3}
192	5.2083×10^{-3}	1.24×10^{-3}	3.36×10^{-4}	9.02×10^{-3}	5.00×10^{-3}

The DNS error with respect to the exact oscillatory solution remains of order 10^{-3} in L^∞ and about 4×10^{-4} in L^2, and is essentially independent of the mesh size in this range, confirming that the FV–RK discretization has reached a regime where the temporal and spatial errors are

well controlled for $h < \varepsilon$. The numerical homogenized solution u^h is noticeably less accurate with respect to u^ε, with L^∞–errors around 9×10^{-3} and L^2–errors around 5×10^{-3} that are also nearly mesh–independent; this reflects the intrinsic modeling error of homogenization when the microscopic oscillations are still resolved by the mesh and thus physically visible in the DNS solution.

To visualize these effects, we display in Figures 7–9 the 2D profiles of $u^{\varepsilon h}$, u^ε and u^h and their cross–sections for a representative pre–homogenization configuration, e.g. $N = 64$, $\varepsilon = 1.5 \times 10^{-1}$. The DNS solution reproduces the oscillatory pattern of the exact solution, while the homogenized solution remains smooth and misses the fine–scale variations.

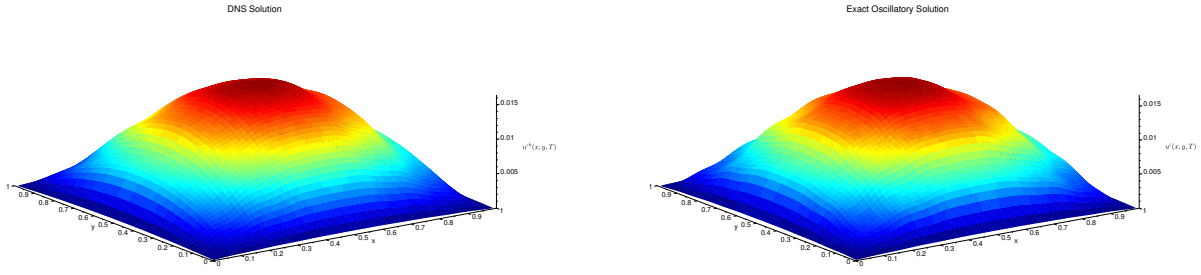

Figure 7: Two–dimensional DNS solution $u^{\varepsilon h}(x, y, T)$ (left) and exact oscillatory solution $u^\varepsilon(x, y, T)$ (right) in the pre–homogenization regime with $\varepsilon = 1.5 \times 10^{-1}$ and $h < \varepsilon$.

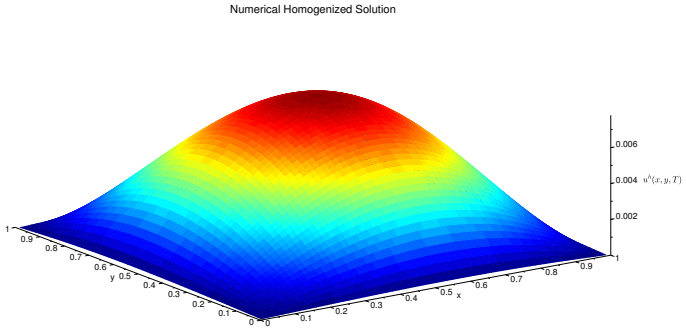

Figure 8: Two–dimensional numerical homogenized solution $u^h(x, y, T)$ in the pre–homogenization regime with $\varepsilon = 1.5 \times 10^{-1}$ and $h < \varepsilon$.

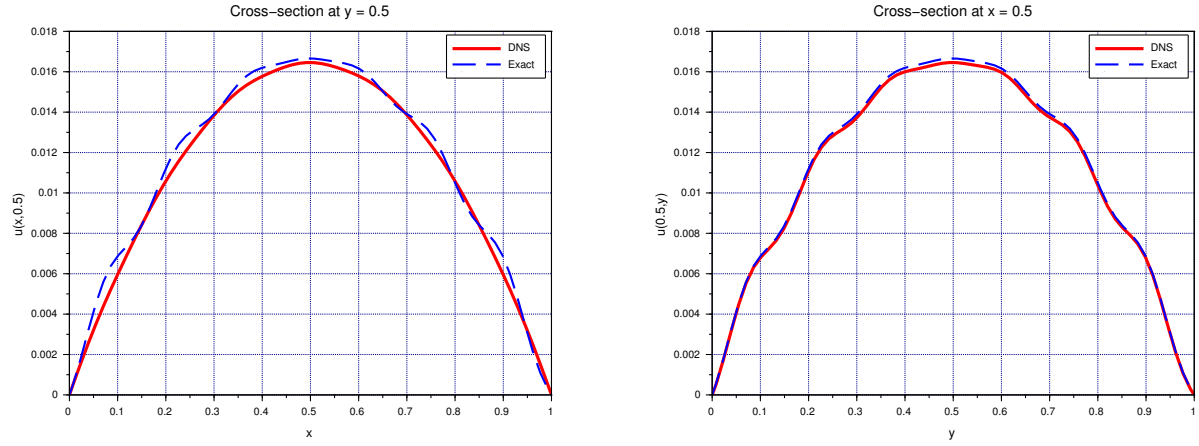

Figure 9: Cross–sections of the 2D solutions in the pre–homogenization regime $\varepsilon = 1.5 \times 10^{-1}$, $h < \varepsilon$. Left: cut at $y = 0.5$, comparison between $u^{\varepsilon h}$ and u^{ε}. Right: cut at $x = 0.5$ for the same three solutions.

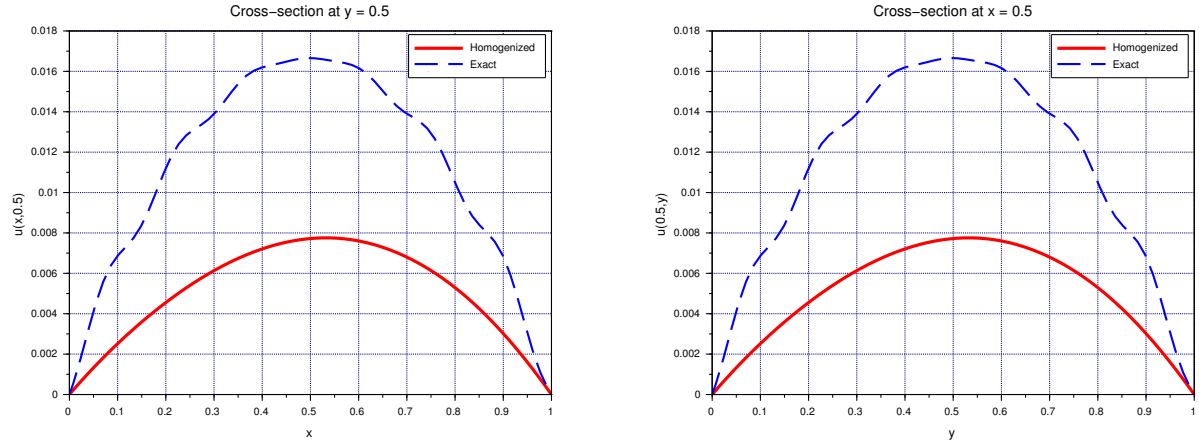

Figure 10: Cross–sections of the 2D solutions in the pre–homogenization regime $\varepsilon = 1.5 \times 10^{-1}$, $h < \varepsilon$. Left: cut at $y = 0.5$, comparison between u^{h} and u^{ε}. Right: cut at $x = 0.5$ for the same three solutions.

4.3.2. *Post–homogenization regime in 2D: $h > \varepsilon$.* We now turn to the post–homogenization regime, where the mesh size is much larger than the microscopic period. In this case the oscillations of the coefficients are not resolved by the grid, and both the DNS for the oscillatory problem and the numerical homogenized solution are expected to approximate the same macroscopic limit.

To construct such a regime, we fix $\varepsilon = \sqrt{2} \times 10^{-5} \approx 1.4142 \times 10^{-5}$ and use again $N \in \{16, 32, 64, 128, 192\}$, so that $h \gg \varepsilon$ in all tests. Table 4.2 reports the errors between u_h^{ε} and u^{ε}, and between u_h^0 and u^{ε}, for these configurations.

In this post–homogenization regime, the DNS error with respect to u^{ε} remains small and essentially constant as N increases, with L^{∞}–errors of order 10^{-3} and L^2–errors of order 10^{-4}. The numerical homogenized solution u^h shows an error of order 8×10^{-3} in L^{∞} and about 4.2×10^{-3} in L^2, again almost independent of N, which confirms that for $\varepsilon \ll h$ the oscillatory solution is very close to its homogenized limit and that the dominant error is of modeling type rather than numerical. Both DNS and homogenized computations thus provide reliable macroscopic approximations of the exact oscillatory solution in this regime.

Table 4.2: 2D post–homogenization regime ($\varepsilon = \sqrt{2} \times 10^{-5}$): errors between the DNS solution $u^{\varepsilon h}$ of the oscillatory problem and the exact oscillatory solution u^{ε}, and between the DNS solution u^h of the homogenized problem and u^{ε}, at final time $T = 1$.

N	h	$\|u^{\varepsilon h} - u^{\varepsilon}\|_{L^\infty}$	$\|u^{\varepsilon h} - u^{\varepsilon}\|_{L^2}$	$\|u^{h} - u^{\varepsilon}\|_{L^\infty}$	$\|u^{h} - u^{\varepsilon}\|_{L^2}$
16	6.25×10^{-2}	8.77×10^{-4}	3.34×10^{-4}	7.93×10^{-3}	4.21×10^{-3}
32	3.125×10^{-2}	8.37×10^{-4}	2.22×10^{-4}	7.94×10^{-3}	4.23×10^{-3}
64	1.5625×10^{-2}	9.16×10^{-4}	2.40×10^{-4}	7.95×10^{-3}	4.23×10^{-3}
128	7.8125×10^{-3}	1.45×10^{-4}	3.88×10^{-5}	7.95×10^{-3}	4.23×10^{-3}
192	5.2083×10^{-3}	1.56×10^{-4}	3.77×10^{-5}	7.95×10^{-3}	4.23×10^{-3}

Figures 11–12 display the corresponding 2D profiles and cross–sections for a representative case, e.g. $N = 64$, $\varepsilon = \sqrt{2} \times 10^{-5}$. One observes that the three curves almost superpose at the macroscopic scale, with only minor discrepancies close to the boundaries, which corroborates the small error levels in Table 4.2.

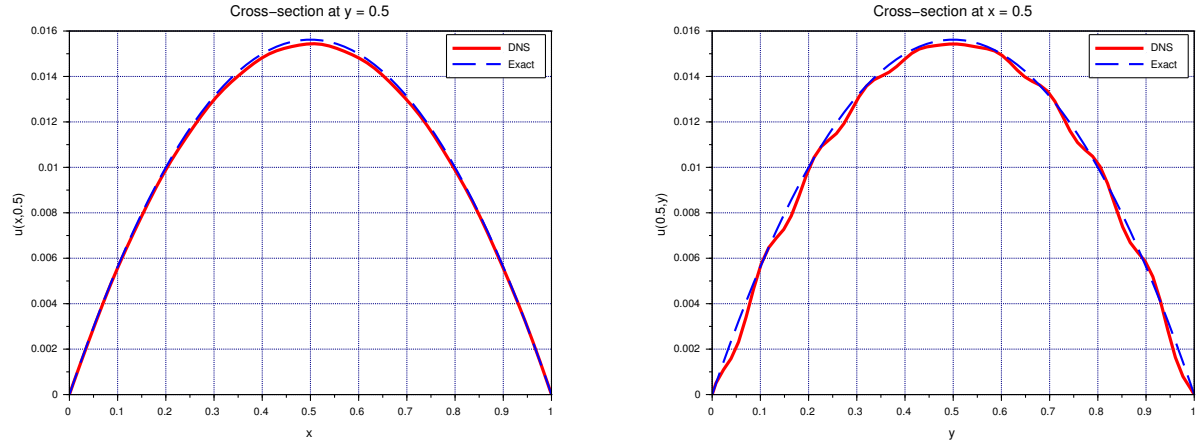

Figure 11: Two–dimensional DNS solution $u^{\varepsilon h}(x, y, T)$ (left) and exact oscillatory solution $u^{\varepsilon}(x, y, T)$ (right) in the post–homogenization regime with $\varepsilon = \sqrt{2} \times 10^{-5}$ and $h > \varepsilon$.

4.3.3. *Convergence as $\varepsilon \to 0$ for fixed mesh size.* In many practical situations, the mesh size h is constrained by computational resources, and it is therefore important to understand how the DNS and homogenized solutions behave when the microscopic scale ε tends to zero while the grid is kept fixed. To address this question, we perform a series of 2D tests with a fixed resolution $N = 64$ (i.e. $h = 1/64 \approx 1.5625 \times 10^{-2}$) and a sequence of decreasing values of ε given by $\varepsilon = \sqrt{2} \times 10^{-k}$, with $k \in \{1, 2, 5, 8, 10\}$.

Table 4.3 reports the corresponding errors between the DNS solution $u^{\varepsilon h}$ and the exact oscillatory solution u^{ε}, and between the numerical homogenized solution u^h and u^{ε}, at the final time $T = 1$. The data clearly show that the DNS error with respect to u^{ε} quickly reaches a plateau as ε decreases, while the discrepancy between u^h and u^{ε} converges to an almost constant value once $\varepsilon \ll h$.

These results indicate that, for a fixed mesh h, the DNS error with respect to u^{ε} does not vanish as $\varepsilon \to 0$, but rather stabilizes at values of order 10^{-3} in L^∞ and between 10^{-4} and 10^{-3} in L^2.This is consistent with the fact that the micro–scale oscillations are not fully resolved when $\varepsilon \ll h$. At the same time, the numerical homogenized solution u^h rapidly approaches a steady macroscopic limit, with errors around 8×10^{-3} in L^∞ and 4.23×10^{-3} in L^2 that

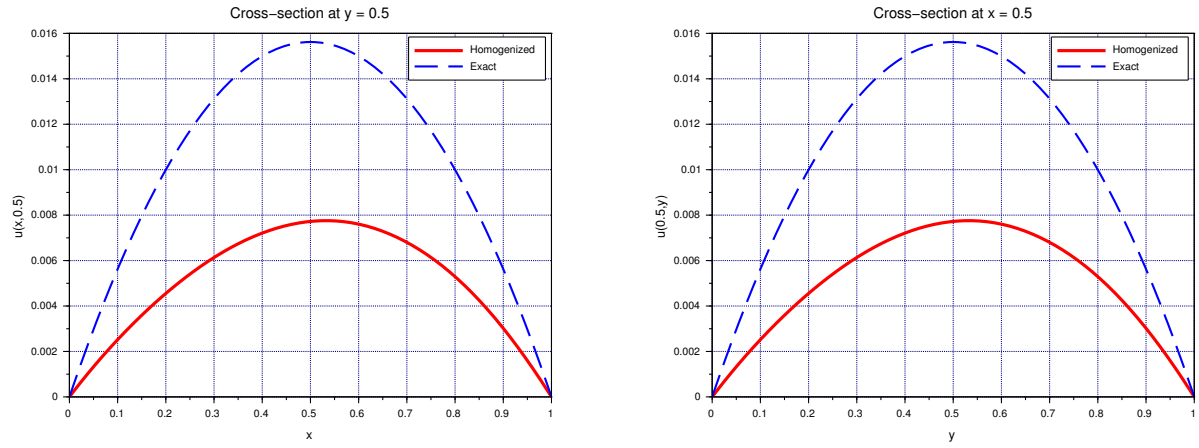

Figure 12: Cross–sections of the 2D solutions in the post–homogenization regime $\varepsilon = \sqrt{2} \times 10^{-5}$, $h > \varepsilon$. Left: cut at $y = 0.5$, comparison between $u^{\varepsilon h}$, u^{ε} and u^{h}. Right: cut at $x = 0.5$ for the same three solutions.

Table 4.3: 2D convergence test as $\varepsilon \to 0$ for fixed mesh size $N = 64$ ($h = 1/64$): errors between the DNS solution $u^{\varepsilon h}$ of the oscillatory problem and the exact oscillatory solution u^{ε}, and between the DNS solution u^{h} of the homogenized problem and u^{ε}, at final time $T = 1$.

ε	$\|u^{\varepsilon h} - u^{\varepsilon}\|_{L^\infty}$	$\|u^{\varepsilon h} - u^{\varepsilon}\|_{L^2}$	$\|u^{h} - u^{\varepsilon}\|_{L^\infty}$	$\|u^{h} - u^{\varepsilon}\|_{L^2}$
$\sqrt{2} \times 10^{-1}$	1.11×10^{-3}	3.25×10^{-4}	8.05×10^{-3}	4.32×10^{-3}
$\sqrt{2} \times 10^{-5}$	9.16×10^{-4}	2.40×10^{-4}	7.95×10^{-3}	4.23×10^{-3}
$\sqrt{2} \times 10^{-8}$	3.83×10^{-4}	9.35×10^{-5}	7.95×10^{-3}	4.23×10^{-3}
$\sqrt{2} \times 10^{-10}$	2.63×10^{-4}	7.77×10^{-5}	7.95×10^{-3}	4.23×10^{-3}

become essentially independent of ε once ε is much smaller than h. This behaviour confirms, in a fully discrete setting, the practical relevance of solving the homogenized problem numerically when $\varepsilon \ll h$, as the homogenized solution provides a robust and efficient approximation of the oscillatory dynamics at the grid scale.

For illustration, one can plot the 2D profiles and cross–sections of $u^{\varepsilon h}$, u^{ε} and u^{h} for the different values of ε on the fixed grid $N = 64$. As ε decreases, the DNS solution becomes visually indistinguishable from its own coarse–scale average, while the numerical homogenized solution remains essentially unchanged, thus capturing the effective large–scale behaviour that is actually visible on the mesh.

4.4. **Discussion of numerical results.** The collection of one– and two–dimensional experiments provides a coherent picture of how direct numerical simulation and homogenized modeling complement each other for oscillatory hyperbolic problems. In all cases, the MOL–FV–RK scheme yields stable and accurate approximations, both for the original microscopic problem and for the homogenized one, which allows us to clearly separate discretization effects from genuine modeling errors due to homogenization.

In the pre–homogenization regime, characterized by $h < \varepsilon$, the numerical results show that the DNS solution of the oscillatory problem closely follows the exact oscillatory solution, while the numerical homogenized solution u^{h} exhibits a significantly larger discrepancy with u^{ε}. This behaviour is observed in both 1D and 2D, and it remains essentially independent of the mesh size once h is sufficiently small, indicating that the dominant error is not of numerical origin

but rather stems from the inability of the homogenized model to reproduce the fine–scale oscillations that are still fully resolved on the computational grid. The 2D tests with $\varepsilon = 1.5 \times 10^{-1}$ confirm that, in this regime, homogenization is not appropriate if one is interested in quantities that are sensitive to the micro–structure, whereas DNS remains reliable at the price of a finer mesh.

In the post–homogenization regime, where $h > \varepsilon$ and the oscillations are under–resolved, both the DNS solution of the oscillatory problem and the numerical homogenized solution approximate the same macroscopic limit. The error tables in 1D and 2D reveal that, for very small ε, the DNS errors are of order 10^{-3} in L^∞ (and between 10^{-4} and 10^{-3} in L^2), while the homogenized solution differs from u^ε by at most a few 10^{-2} in L^∞ with L^2–errors around 4×10^{-3}, and these values remain almost constant as the mesh is refined. This shows that the homogenized model captures the effective dynamics and that further refinement mainly reduces the discretization error of the FV–RK scheme. The 2D computations with $\varepsilon = \sqrt{2} \times 10^{-5}$ illustrate this clearly: the three solutions become visually almost indistinguishable on the plotted cross–sections, and the measured errors stabilize across all values of N.

The additional convergence tests with fixed mesh size and decreasing ε provide further insight into practical situations where the grid cannot be refined arbitrarily. For a fixed resolution $N = 64$, the DNS error with respect to u^ε tends to a non–zero plateau as $\varepsilon \to 0$, reflecting the fact that the microscopic oscillations are largely filtered out by the coarse mesh and cannot be directly resolved. At the same time, the numerical homogenized solution u^h rapidly converges toward a stable macroscopic profile, and its error with respect to u^ε becomes essentially independent of ε once the scale separation is sufficiently strong. These observations confirm the classical homogenization picture in a fully discrete setting and show that, in practice, solving the homogenized problem numerically is the most efficient way to approximate the oscillatory dynamics when $\varepsilon \ll h$.

Another important outcome of the numerical study is the clarification of numerical locking mechanisms when the mesh size h and the microscopic period ε are commensurable. The 1D experiments demonstrate that, for certain ratios h/ε, the discrete sampling can accidentally reproduce the correct homogenized coefficients and lead to a DNS solution that coincides with both the exact oscillatory and homogenized solutions, while for other ratios the same mechanism produces completely incorrect results that are unrelated to either reference solution. This sensitivity to commensurability underscores the need for careful mesh design in multiscale computations: choosing h so that h/ε lies in a "resonant" set may induce spurious locking, whereas avoiding such ratios leads to robust and predictable behaviour. Although the 2D tests considered here do not exhibit dramatic locking phenomena for the chosen coefficients, the underlying mechanism remains the same and must be kept in mind in more complex configurations.

From a practical standpoint, the combined 1D and 2D results support a simple strategy for multiscale hyperbolic problems with oscillatory coefficients. When ε is comparable to h or larger, and when microscopic details matter, one should rely on direct finite–volume simulation of the original problem, using sufficiently fine meshes and possibly adaptive refinement near regions of interest. When ε is much smaller than the accessible mesh size, numerical homogenization of the effective problem provides an accurate and computationally efficient alternative, with errors that are dominated by the modeling approximation rather than by discretization. The error atlas constructed in this work, together with the identification of locking regimes, thus offers concrete guidelines on how to choose h relative to ε and on when to prefer DNS or homogenized simulations in real applications.

5. CONCLUSION

This work has presented a systematic numerical comparison between direct finite–volume simulation and homogenized modeling for second–order hyperbolic equations with rapidly oscillating coefficients. Using a unified MOL–FV–RK framework in one and two space dimensions, and manufactured solutions allowing exact error measurements, several asymptotic regimes and numerical pathologies have been quantified.

In the pre–homogenization regime, where the mesh size is smaller than the microscopic period, the direct scheme accurately captures the oscillatory solution, while the homogenized model exhibits a non–negligible bias due to the loss of fine–scale information.
In the post–homogenization regime, with $\varepsilon \ll h$, both DNS and homogenized solutions provide excellent approximations of the exact oscillatory solution, and their errors remain small and nearly independent of the mesh size, both in 1D and 2D. The numerical experiments further highlight the possibility of numerical locking when h and ε are commensurable, and the analysis clarifies how suitable choices of mesh size and coefficients can either avoid or deliberately illustrate this phenomenon.

From an application standpoint, these results emphasize that homogenization and DNS should be viewed as complementary rather than competing tools. Homogenized models are well suited for strongly separated scales and macroscopic predictions, while DNS remains indispensable whenever microscopic features are of physical relevance or when the scale separation is only moderate. The finite volume methodology developed here, together with the error atlas across (h, ε), offers practical guidelines for the robust numerical simulation of multiscale hyperbolic problems in heterogeneous media. Possible extensions include the treatment of non–diagonal diffusion tensors, nonlinear source terms, and more complex boundary conditions, as well as the design of adaptive strategies that automatically select between DNS and homogenized models based on local scale indicators.

REFERENCES

[1] B. AMAZIANE, and B. ONDAMI, Numerical approximations of a second order elliptic equation with highly oscillating coefficients, *Notes Numer. Fluid Mech.* **70** (1999), pp. 1–11.

[2] G. ALLAIRE, Introduction to homogenization theory, CEA–EDF–INRIA School on Homogenization, 13–16 December 2010, `http://www.cmap.polytechnique.fr/allaire/homog/lect1.pdf`.

[3] G. ALLAIRE, Homogenization and two-scale convergence, *SIAM J. Math. Anal.* **23**(6) (1992), pp. 1482–1518.

[4] G. ALLAIRE, *Shape Optimization by the Homogenization Method*, Springer, Berlin, (2002).

[5] D. J. BAMBI PEMBA, Sur l'approximation numérique par la méthode des volumes finis de quelques problèmes d'écoulements en milieux poreux hétérogènes, à structures périodiques, Thèse de Doctorat, Université Marien Ngouabi, Brazzaville, (2024).

[6] D. J. BAMBI PEMBA and B. ONDAMI, Finite volume approximation of a class of 2D elliptic equations with discontinuous and highly oscillating coefficients, *Aust. J. Math. Anal. Appl.* **21**(1) (2024), Art. 13, 20 pp.

[7] D. J. BAMBI PEMBA and B. ONDAMI, Finite volume approximation of a class of two-dimensional parabolic equations with discontinuous and highly oscillating coefficients, *Int. J. Numer. Methods Appl.* **23**(1) (2023), pp. 51–65.

[8] D. J. BAMBI PEMBA and B. ONDAMI, Numerical approximation by the method of line with finite-volume approach of a solute transport equation in periodic heterogeneous porous medium, *Aust. J. Math. Anal. Appl.* **17**(2) (2020), Art. 6, 18 pp.

[9] T. BARTH, R. HERBIN and M. OHLBERGER, Finite volume methods: foundation and analysis, in: R. Eymard, J.-M. Hérard (eds.), *Finite Volumes for Complex Applications VIII*, Springer Proc. Math. Stat. **200** (2017), pp. 1–70.

[10] A. BENSOUSSAN, J.-L. LIONS and G. PAPANICOLAOU, *Asymptotic Analysis for Periodic Structures*, Amer. Math. Soc., Providence, RI, (2011).

[11] Z. CHEN and T. Y. HOU, A mixed multiscale finite element method for elliptic problems with oscillating coefficients, *Math. Comp.* **72**(242) (2002), pp. 541–576.

[12] D. CIORANESCU and P. DONATO, *An Introduction to Homogenization*, Oxford Univ. Press, Oxford, (1999).

[13] W. DENG and J. HUANG, Upscaling methods for a class of convection–diffusion equation with highly oscillating coefficients, *J. Comput. Phys.* **227** (2008), pp. 7621–7642.

[14] D. ESTEP, M. PERNICE, D. PHAM, S. TAVENER and H. WANG, A posteriori error analysis of a cell-centered finite volume method for semilinear elliptic problems, *J. Comput. Appl. Math.* **233** (2009), pp. 459–472.

[15] R. EYMARD, T. GALLOUËT and R. HERBIN, The finite volume method, in: P. G. Ciarlet, J.-L. Lions (eds.), *Handbook of Numerical Analysis, Vol. 7*, North-Holland, Amsterdam, (2000), pp. 713–1020.

[16] U. HORNUNG, *Homogenization and Porous Media*, Springer, New York, (1997).

[17] V. V. JIKOV, S. M. KOZLOV and O. A. OLEINIK, *Homogenization of Differential Operators and Integral Functionals*, Springer, Berlin, (1994).

[18] Yu. M. MESHKOVA and T. A. SUSLINA, Homogenization of initial boundary-value problem for parabolic systems: operator error estimates, *Algebra i Analiz* **29**(6) (2017), 99–158; English transl.: *St. Petersburg Math. J.* **29**(6) (2018).

[19] Yu. M. MESHKOVA and T. A. SUSLINA, Homogenization of initial boundary value problems for parabolic systems with periodic coefficients, *Appl. Anal.* **95**(8) (2016), pp. 1736–1775.

[20] B. ONDAMI, Finite volume discretization of a class of parabolic equations with discontinuous and oscillating coefficients, *Appl. Math. Sci.* **12**(3) (2018), pp. 121–135.

[21] B. ONDAMI, Approximation of a second-order elliptic equation with discontinuous and highly oscillating coefficients by finite volume methods, *J. Math. Res.* **8**(6) (2016), pp. 34–44.

[22] B. ONDAMI, The effect of numerical integration on the finite element approximation of a second order elliptic equation with highly oscillating coefficients, *J. Interpol. Approx. Sci. Comput.* **2** (2015), pp. 128–136.

[23] B. ONDAMI, Sur quelques problèmes d'homogénéisation des écoulements en milieux poreux, Thèse de Doctorat, Université de Pau et des Pays de l'Adour, France, (2001).

[24] SCILAB ONLINE HELP, `https://help.scilab.org/docs/6.1.1/fr_FR/ode.html`, (2024).

[25] T. A. SUSLINA, Homogenization of a periodic parabolic Cauchy problem, in: *Nonlinear Equations and Spectral Theory*, Amer. Math. Soc. Transl. Ser. 2, **220** (2007), pp. 201–233.

[26] G. ALLAIRE, *Introduction to Homogenization Theory*, CEA–EDF–INRIA School on Homogenization, 13–16 December 2010, `http://www.cmap.polytechnique.fr/~allaire/homog/lect1.pdf`.

[27] Y. EFENDIEV and T. Y. HOU, *Multiscale Finite Element Methods: Theory and Applications*, Surv. Tutor. Appl. Math. Sci. **4**, Springer, New York, (2009).

[28] J. B. DIAZ and F. T. METCALF, A complementary triangle inequality in Hilbert and Banach spaces, *Proc. Amer. Math. Soc.*, **17** (1966), pp. 88–97.

[29] S. S. DRAGOMIR, New reverses of Schwarz, triangle and Bessel inequalities in inner product spaces, *Aust. J. Math. Anal. Appl.*, **1** (2004), No. 1, Article 1, [Online: https://ajmaa.org/cgi-bin/paper.pl?string=v1n1/nrstbiips.tex].

[30] D. S. MITRINOVIĆ, J. E. PEČARIĆ and A. M. FINK, *Classical and New Inequalities in Analysis*, Kluwer Academic Publishers, Dordrecht, 1993.